

# Long-term Scintillation Observations of Five Pulsars at 1540 MHz

N. Wang,<sup>1,2,3\*</sup> R. N. Manchester,<sup>3</sup> S. Johnston,<sup>2</sup> B. Rickett,<sup>4</sup> J. Zhang,<sup>1</sup>  
A. Yusup,<sup>1</sup> M. Chen<sup>1</sup>

<sup>1</sup> *National Astronomical Observatories, CAS, 40-5 South Beijing Road, Urumqi, 830011, China*

<sup>2</sup> *School of Physics, University of Sydney, NSW 2006, Australia*

<sup>3</sup> *Australia Telescope National Facility, CSIRO, PO Box 76, Epping, NSW 1710, Australia*

<sup>4</sup> *Department of Electrical and Computer Engineering, University of California, San Diego, USA*

24 September 2018

## ABSTRACT

From 2001 January to 2002 June, we monitored PSRs B0329+54, B0823+26, B1929+10, B2020+28 and B2021+51 using the Nanshan 25-m radio telescope of Urumqi Observatory to study their diffractive interstellar scintillation (DISS). The average interval between observations was about 9 days and the observation duration ranged between 2 and 6 hours depending on the pulsar. Wide variations in the DISS parameters were observed over the 18-month data span. Despite this, the average scintillation velocities are in excellent agreement with the proper motion velocities. The average two-dimensional autocorrelation function for PSR B0329+54 is well described by a thin-screen Kolmogorov model, at least along the time and frequency axes. Observed modulation indices for the DISS time scale and bandwidth and the pulsar flux density are greater than values predicted for a Kolmogorov spectrum of electron density fluctuations. Correlated variations over times long compared to the nominal refractive scintillation time are observed, suggesting that larger-scale density fluctuations are important. For these pulsars, the scintillation bandwidth as a function of frequency has a power-law index ( $\sim 3.6$ ) much less than expected for Kolmogorov turbulence ( $\sim 4.4$ ). Sloping fringes are commonly observed in the dynamic spectra, especially for PSR B0329+54. The detected range of fringe slopes are limited by our observing resolution. Our observations are sensitive to larger-scale fringes and hence smaller refractive angles, corresponding to the central part of the scattering disk.

**Key words:** – ISM:general – ISM:structure – pulsars:general

## 1 INTRODUCTION

Diffractive interstellar scintillation (DISS) occurs when radiation from a pulsar has phase fluctuations imposed on it due to small scale variations in the interstellar electron density. The scattered rays interfere constructively and destructively, resulting in a modulation of the pulse intensity as a function of frequency and position on the observer plane. Pulsars are good probes of DISS because of their very small angular size. The relative motion of the pulsar, scattering material and the observer transforms the spatial variation into a time variation of the signal intensity. The modulation is characterized by a timescale ( $\Delta t_d$ ) of minutes to hours and a decorrelation frequency scale ( $\Delta \nu_d$ ) over a wide frequency

range from kHz to MHz, with distant pulsars scintillating faster in both frequency and time (Cordes, Pidwerbetsky & Lovelace 1986; Gupta, Rickett & Lyne 1994; Bhat, Rao & Gupta 1999). Longer-term fluctuations in pulsar flux densities result from a focussing and defocussing of the ray bundle due to larger-scale inhomogeneities in the interstellar electron density. This phenomenon, known as refractive interstellar scintillation (RISS), is broad-band and shows less modulation in distant pulsars.

By analogy with neutral gas turbulence theory, the density fluctuations in the ionized interstellar medium (ISM) can be described by a power-law spectrum. The three-dimensional spatial power-law spectrum is of the form:

$$P_{3n} = C_n^2 q^{-\beta} \quad (1)$$

where  $C_n^2$  is a measurement of the mean turbulence of electron density along the line of sight and  $q = 2\pi/s$  is the

\* Email: na.wang@ms.xjb.ac.cn

wavenumber associated with the spatial scale of turbulence  $s$ . The spatial scale  $s$  is in the range of  $s_{\text{inn}} \ll s \ll s_{\text{out}}$ , where  $s_{\text{inn}}$  and  $s_{\text{out}}$  correspond to the inner and outer scales of the density fluctuations. The index  $\beta$  is thought to lie in the range  $3 < \beta < 5$ . For propagation of turbulent energy from large scales to small scales, the well-known Kolmogorov theory of turbulence gives a value of  $\beta = 11/3$ . Observations show that this generally applies in the interstellar medium between scales of  $s_{\text{out}} \sim 10^{17} - 10^{19}$  cm and  $s_{\text{inn}} \sim 10^8 - 10^{10}$  cm (Spangler & Gwinn 1990; Kaspi & Stinebring 1992; Armstrong, Rickett & Spangler 1995; Bhat, Gupta & Rao 1999).

There are discrepancies in the observed scintillation spectra compared to the predictions of Kolmogorov turbulence (Gupta, Rickett & Coles 1993). For example, modulation depths and time scales often do not scale according to the Kolmogorov model. Various modifications to the Kolmogorov model have been proposed, including the steep spectrum model ( $\beta \geq 4$ ) (Blandford & Narayan 1985; Goodman & Narayan 1985) and the inner scale model are notable. The steep spectrum model does not require a turbulent cascade; it could result from the superposition of noninteracting discrete structures in space. The inner scale model has a cutoff at the scale at which the turbulent energy dissipates (Coles et al. 1987).

The variation in observed pulsar flux density as a function of time and frequency is known as the dynamic spectrum and the interference maxima in the dynamic spectrum are called scintles. Decorrelation time scale and bandwidth are parameters which quantify the scintle size. A simplified model is often used in which a thin scattering disk is assumed to lie midway between the pulsar and observer. In general this is in good agreement with observations. For a pulsar at distance  $D$  from the Earth, the decorrelation time scale for DISS has the form of

$$\Delta t_d \propto \nu^{2/(\beta-2)} D^{-1/(\beta-2)} V_s^{-1} \quad (\beta < 4), \quad (2)$$

$$\Delta t_d \propto \nu^{(\beta-2)/(6-\beta)} D^{-(\beta-3)/(6-\beta)} V_s^{-1} \quad (\beta > 4), \quad (3)$$

where  $\nu$  is the radio frequency (Rickett 1977; Goodman & Narayan 1985). In particular, for a Kolmogorov spectrum,

$$\Delta t_d \propto \nu^{6/5} D^{-3/5} V_s^{-1}. \quad (4)$$

The decorrelation bandwidth for DISS is

$$\Delta \nu_d \propto \nu^{2\beta/(\beta-2)} D^{-\beta/(\beta-2)} \quad (\beta < 4), \quad (5)$$

$$\Delta \nu_d \propto \nu^{8/(6-\beta)} D^{-\beta/(6-\beta)} \quad (\beta > 4) \quad (6)$$

(Rickett 1977; Goodman & Narayan 1985). In the Kolmogorov case,

$$\Delta \nu_d \propto \nu^{22/5} D^{-11/5}. \quad (7)$$

Equations 2 to 7 indicate that fluctuations are more rapid and have narrower bandwidths for more distant pulsars and at lower frequencies.

In the Kolmogorov case, the scaling factor  $C_n^2$  is given by

$$C_n^2 \approx 0.002 \nu^{11/3} D^{-11/6} \Delta \nu_d^{-5/6}, \quad (8)$$

where  $\nu$  is in GHz,  $D$  is in kpc,  $\Delta \nu_d$  is in MHz and  $C_n^2$  is in units of  $\text{m}^{-20/3}$  (Cordes 1986).

Quasi-periodic fringes resulting from interference between multiple images of the pulsar by the scattering screen, are often observed in dynamic spectra (Hewish, Wolszczan & Graham 1985; Wolszczan & Cordes 1987; Bhat, Rao & Gupta 1999), with broad and narrow fringes indicating small and large separations of the ray paths (or images) respectively. The fringes are generally sloped on the dynamic spectra, i.e., periodic in both frequency and time and crossed fringes (i.e., slopes of both signs) are common. Such sloped fringes result from motion of the fringe pattern across the observer plane due to relative motion of the pulsar, Earth and the scattering screen. In the case of an equivalent thin screen located approximately midway between the pulsar and the observer, the maximum fringe slope is given by

$$\frac{dt}{d\nu} = \frac{D \theta_r}{V_s \nu} \quad (9)$$

where  $\theta_r$  is the refraction angle and  $V_s$  is the velocity of the fringe pattern across the observer plane, normally dominated by the pulsar velocity (Hewish 1980; Bhat, Gupta & Rao 1999). The refractive angle  $\theta_r$  is approximately proportional to  $\nu^{-2}$  for a given gradient in refractive index. Therefore, for large-scale gradients, the fringe slope  $dt/d\nu$  might be expected to vary approximately as  $\nu^{-3}$ . For different projections of the velocity on the line between the images, the slope varies in magnitude and sign, resulting in crossed fringes of varying slope. Earlier papers discussed Equation 9 in terms of the frequency dependence of the refraction angle (e.g. Gupta, Rickett & Lyne, 1994), but this equation results directly from consideration of the geometric delays. For interference between a strong central image and other points within the midplaced scattering disk, the fringe rates in frequency ( $f_\nu$ ) and time ( $f_t$ ) are related by

$$f_\nu = \frac{D}{2c\nu^2 V_s^2} f_t^2, \quad (10)$$

where  $c$  is speed of light (Stinebring et al. 2001), and  $V_s$  is dominated by the pulsar proper motion. This shows that crossed fringe patterns transform to parabolic arc structures in the ‘secondary spectrum’, that is, the two-dimensional Fourier transform of the dynamic spectrum. Such parabolic arcs and other more complex structures have been observed in a number of pulsars (Hill et al. 2003).

In this paper, we describe observations of five pulsars (PSRs B0329+54, B0823+26, B1929+10, B2020+28 and B2021+51). In Section 2 we introduce the observations and data analysis. Section 3 presents the dynamic spectra and in Section 4 & 5 we show the auto-correlation functions and describe the time variations of the scintillation parameters. Secondary spectra for PSR B0329+54 are presented in Section 6. In Section 7 we discuss our results and compare them with previous observations and the predictions of scintillation theories, and Section 8 summarises the results.

## 2 OBSERVATIONS AND DATA ANALYSIS

The observations were made by using the Nanshan 25-m telescope, operated by Urumqi Observatory, National Astronomical Observatories of China. The pulsars were regularly monitored from 2001 January to 2002 June with an average interval between observations of nine days. Our observations were centred at 1540 MHz, a relatively high frequency at

which pulsar scintillation properties have not been well studied. Most earlier observations (e.g., Cordes, Wesberg & Borikoff 1985; Gupta, Rickett & Lyne 1994; Bhat, Rao & Gupta 1999) were less frequent and centred on lower frequencies, 327, 408 and 610 MHz. The receiver was a dual-polarisation room-temperature system with noise temperature of 95 K, equivalent to a system flux density of 1080 Jy. Frequency resolution was provided by a filterbank system consisting of 128 channels with channel bandwidths of 2.5 MHz giving a total bandwidth of 320 MHz for each polarisation. This system was described in more detail by Wang et al. (2001). The data were folded online and saved to disk every four minutes. Total integration time was from three to six hours, depending on the pulsar scintillation time scale  $\Delta t_d$ . We made 6-hour observations for the closer pulsars, PSRs B1919+10, B2020+28 and B2021+51, while the observations were three hours for the more distant pulsars PSRs B0329+54 and B0823+26. Between 38 and 65 observations were made of each pulsar. We calibrated the pulsar flux density scale using ten strong, relatively distant pulsars which all have well-measured flux densities in the pulsar catalogue.

Parameters for the observed pulsars are listed in Table 1. Column 3 gives the pulsar dispersion measure and column 4 gives the pulsar distances obtained from parallax observations. Uncertainties in the last quoted digit are given in parentheses. Column 5 gives the transverse velocities based on measured proper motion and the parallax distance. Columns 6 and 7 give the pulsar Galactic longitude and latitude respectively, and pulsar distances from the Galactic plane are given in last column.

To get the dynamic spectrum, we first dedispersed and summed the data for each observation to determine the pulse phase at the centre frequency. Pulse intensities were then determined for each sub-integration and each frequency channel by summing the data within phase  $\pm 0.05$  of the predicted phase of the pulse peak and subtracting a baseline offset.

Persistent narrow-band interference was found in frequency ranges 1465–1472 MHz, 1482–1490 MHz, 1522–1527 MHz, 1545–1557 MHz and 1620–1625 MHz; in total about 15% of the frequency channels were affected. We used a linear interpolation across affected channels to remove the interference from the dynamic spectra. Occasionally, impulsive broad-band interference which lasted a few minutes was observed; a similar interpolation was used to remove it.

### 3 DYNAMIC SPECTRA

In this section we present dynamic spectra for PSRs B0329+54, B0823+26, B1929+10, B2020+28 and B2020+51. Spectra selected to show the range of observed features for each pulsar are given in Fig. 1 to Fig. 5. The observing start time, pulsar name and MJD are given at the top of the each spectrum.

#### 3.1 PSR B0329+54

PSR B0329+54 is the strongest northern pulsar with a distance of 1.06 kpc. At 1540 MHz, the pulsar scintillates with typical time scales of 10 – 30 min and decorrelation bandwidths of 5 – 15 MHz. We observed PSR B0329+54 at 64

epochs over the 18-month interval, with a typical observation time of three hours. Fig. 1 shows 12 of the dynamic spectra which have been corrected for both the short broad-band interference and the longer-term narrow-band interference.

The dynamic spectra shown in Fig. 1 reveal very different properties compared to the lower frequency observations reported by Gupta, Rickett & Lyne (1994) and Stinebring, Faison & McKinnon (1996) which were at 408 MHz and 610 MHz respectively. There is a much wider variation in scintillation time-scales and bandwidths from day to day in the 1540 MHz data and many spectra show multiple fringes, which are usually sloping, for example, the dynamic spectra obtained on MJDs 52068.6, 52078.3, 52082.1, 52131.1 and 52202.5. Broad and narrow fringes are often seen at the same time, and these often have opposite slopes. Examples are spectra for MJDs 52027.4, 52078.3 and 52082.1. The dynamic spectrum for MJD 51972.4 is interesting in that it has narrow vertical fringes.

#### 3.2 PSR B0823+26

In total we obtained 48 dynamic spectra for PSR B0823+26, and Fig. 2 shows 4 of them. This pulsar has a distance of 0.38 kpc and a large transverse velocity of  $194 \text{ km s}^{-1}$ . These parameters result in a wide decorrelation bandwidth and a short decorrelation time scale. As will be discussed in Section 7, the average scintillation scale of PSR B0823+26 is about 13 min and the decorrelation bandwidth is about half the receiver bandwidth. As seen with other pulsars the scintle time-scale is shorter than the interval between scintles at a given frequency.

Despite the frequency difference between our observations and those of Gupta, Rickett & Lyne (1994) at 408 MHz and Bhat, Rao & Gupta (1999) at 327 MHz, the dynamic spectra shown in Fig. 2 are similar with large fractional decorrelation bandwidths and slow drifting. The character of the dynamic spectra often change dramatically over short time intervals, for example, from a very broad single scintle to multiple sloping scintles in observations on MJDs 52068.5 and 52078.4 respectively. Clear reversals in the direction of drift slope are seen in observations made just one week apart, e.g., those on MJDs 52249.0 and 52256.0.

#### 3.3 PSR B1929+10

We obtained dynamic spectra for PSR B1929+10 at 38 epochs. This pulsar, with distance of 0.33 kpc, scintillates slowly and its decorrelation bandwidth is obviously comparable to or wider than the receiver bandwidth. As shown in Fig. 3, the six-hour observations typically were able to cover only one or two scintles in the time domain. Features of the spectra at 1540 MHz are very similar to those observed at lower frequencies by Gupta, Rickett & Lyne (1994).

#### 3.4 PSR B2020+28

We observed 52 dynamic spectra for PSR B2020+28. At earlier stages most of the observations were about 3 hours but later we commenced 6-hour observations in order to cover several scintles in each observation. In Fig. 4 we present 4

**Table 1.** Parameters for the observed pulsars.

PSR J	PSR B	DM (pc cm <sup>-3</sup> )	Parallax dist (kpc)	$V_{\text{pm}}$ (km s <sup>-1</sup> )	$l$ (deg)	$b$ (deg)	$z$ (kpc)
(1)	(2)	(3)	(4)	(5)	(6)	(7)	(8)
0332+5434	0329+54	26.84	1.06(12) <sup>a</sup>	98(11) <sup>a</sup>	145.00	-1.22	-0.02
0826+2637	0823+26	19.45	0.38(8) <sup>b</sup>	194(41) <sup>c</sup>	196.96	31.74	0.20
1932+1059	1929+10	3.18	0.33(1) <sup>a</sup>	163(5) <sup>a</sup>	47.38	-3.88	-0.02
2022+2854	2020+28	24.64	2.7(9) <sup>a</sup>	307(103) <sup>a</sup>	68.86	-4.67	-0.22
2022+5154	2021+51	22.65	2.0(3) <sup>a</sup>	119(18) <sup>a</sup>	87.86	8.38	0.29

<sup>a</sup> Briskin et al. (2002)

<sup>b</sup> Gwinn et al. (1986)

<sup>c</sup> Lyne, Anderson & Salter, (1982)

dynamic spectra. Despite its DM of 24.6 pc cm<sup>-3</sup> and a distance of 2.7 kpc, PSR B2020+28 shows rather broad scintles in both time and frequency.

### 3.5 PSR B2021+51

As for PSR B2020+28, PSR B2021+51 initially was observed for three hours each day; from mid-November 2001 observation times were increased to six hours. Altogether we observed 65 dynamic spectra for this pulsar, and 8 examples are shown in Fig. 5. Clear drifting bands were observed on several occasions, for example, the first observed dynamic spectrum at MJD 52016.2. This pulsar shows two types of dynamic spectrum. In some cases the scintles are broad in both frequency and time (e.g., at MJD 52302.3), whereas in other cases the scintles are narrower (e.g., at MJD 52269.5). There appears to be a correlation between signal strength and scintillation type, with the pulsar generally being weaker when the scintles are narrow.

## 4 SCINTILLATION PARAMETERS AND FLUX DENSITIES

### 4.1 Auto-correlation functions

The parameters of DISS can be obtained by forming a two-dimensional auto-correlation function (ACF) of the dynamic spectra  $S(\nu, t)$ , i.e., the pulsar flux density at frequency  $\nu$  and time  $t$ . The ACF is defined by

$$F(\Delta\nu, \Delta t) = [N(\Delta\nu, \Delta t)]^{-1} \sum_{\nu} \sum_t \Delta S(\nu, t) \Delta S(\nu + \Delta\nu, t + \Delta t), \quad (11)$$

where  $\Delta S(\nu, t) = S(\nu, t) - \bar{S}$ , and  $\bar{S}$  is the mean pulsar flux density over each observation.  $N(\Delta\nu, \Delta t)$  is the number of correlated pixel pairs. The normalised ACF is then given by:

$$\rho(\Delta\nu, \Delta t) = F(\Delta\nu, \Delta t) / F(0, 0). \quad (12)$$

We note that in Cordes (1986) the flux density was normalised by subtracting the mean over each sub-integration to minimise the effect of long-term variations, i.e.,  $\Delta S(\nu, t) = S(\nu, t) - \bar{S}(t)$ . However this method can only be applied to spectra that contain many scintles, since in this case the sub-integration mean is close to the global

mean apart from long-term variations. Because of our higher observation frequency, the number of scintles is often small and subtracting the mean from each sub-integration would affect the diffractive parameters.

Four examples of normalised two-dimensional ACFs and one-dimensional cuts at zero lag are plotted in Fig. 6 for each of the five pulsars. Following convention, the scintillation time scale  $\Delta t_d$  is defined as the time lag at zero frequency lag at the point where the ACF is 1/e of the maximum, and the decorrelation frequency scale  $\Delta\nu_d$  is defined as the half-width at half-maximum of the ACF along the frequency lag axis at zero time lag (Cordes 1986). The ACFs show spikes at zero time and frequency lag. These spikes are due to noise in the dynamic spectra, and are more significant for weaker pulsars. Slightly wider spikes resulting from the interference excision process are often also present around zero frequency lag. To remove these spikes we used the neighbouring frequency-lag points to fit for a parabola across zero frequency lag. The central points are interpolated from this fit.

### 4.2 Scintillation parameters

We estimated the diffractive scintillation parameters for each observation by fitting a two-dimensional elliptical Gaussian function (Bhat, Rao & Gupta 1999) to the smoothed ACF using the non-linear least-squares fitting routine LMM. The Gaussian function has the form:

$$C_g(\nu, t) = C_0 \exp(C_1 \nu^2 + C_2 \nu t + C_3 t^2), \quad (13)$$

where  $C_0$  is held fixed to unity as the ACF is normalised. The scintillation parameters  $\Delta t_d$  and  $\Delta\nu_d$  are then given by:

$$\Delta t_d = \left( \frac{1}{C_3} \right)^{0.5}, \quad \Delta\nu_d = \left( \frac{\ln 2}{C_1} \right)^{0.5}. \quad (14)$$

Fig. 6 shows that the Gaussian function represents the observed ACFs well in most cases, although it may not be very reliable when the decorrelation bandwidth is wider than the receiver bandwidth, as in most observations of PSR B1929+10. Time variations of  $\Delta t_d$  and  $\Delta\nu_d$  from all observations of the five pulsars are shown in Fig. 7 to Fig. 11 and average values are given in columns 2 and 3 of Table 2. One-sigma error estimates from the least-squares fit are plotted on each point in the figure. Errors in the table are one-sigma uncertainties in the mean values, assuming a normal

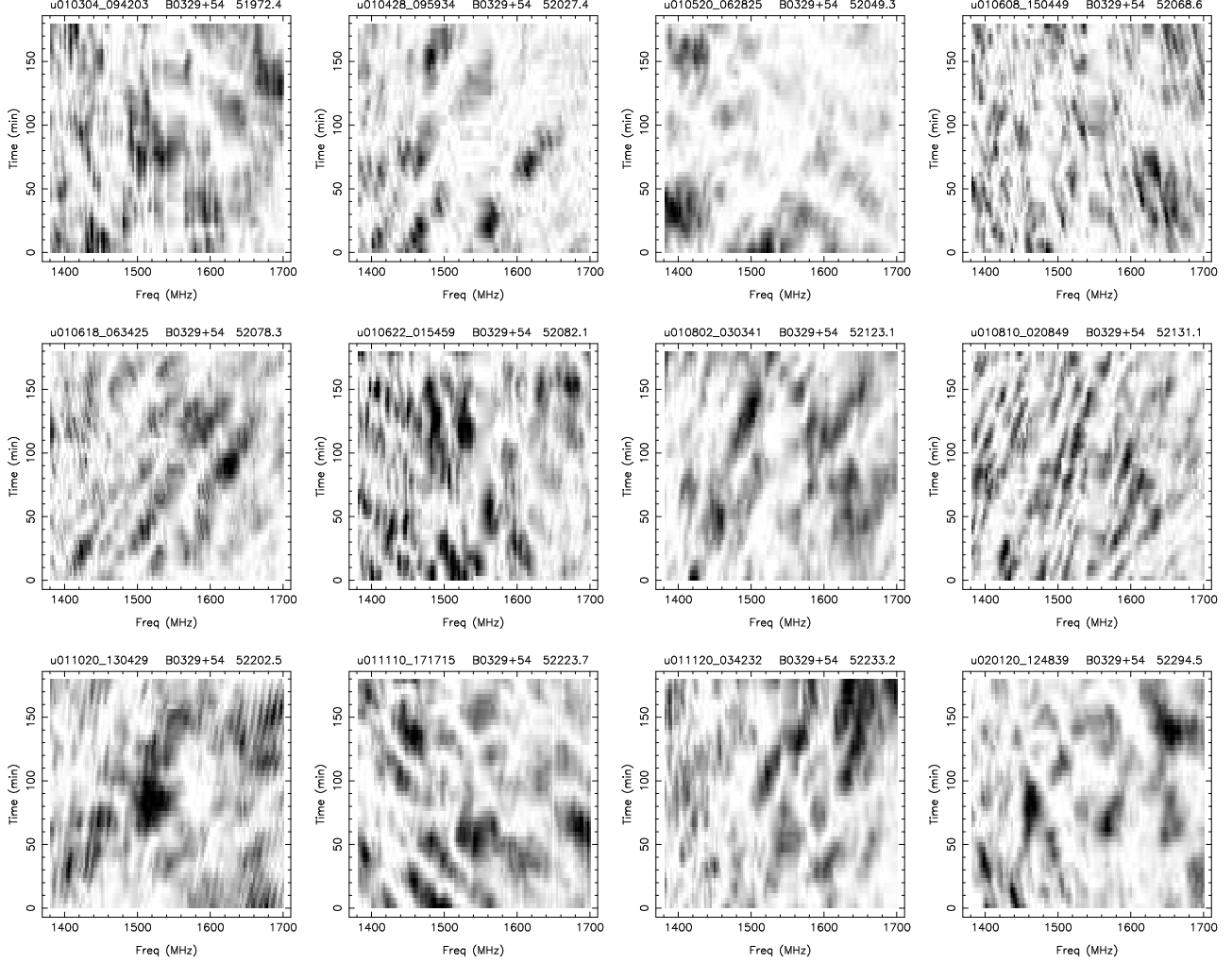


**Figure 1.** Dynamic spectra for PSR B0329+54 at center frequency 1540 MHz, with frequency and time resolution of 2.5 MHz and 4 min respectively. Intensity is represented by a linear greyscale between 1% (white) and 85% (black) of the maximum.

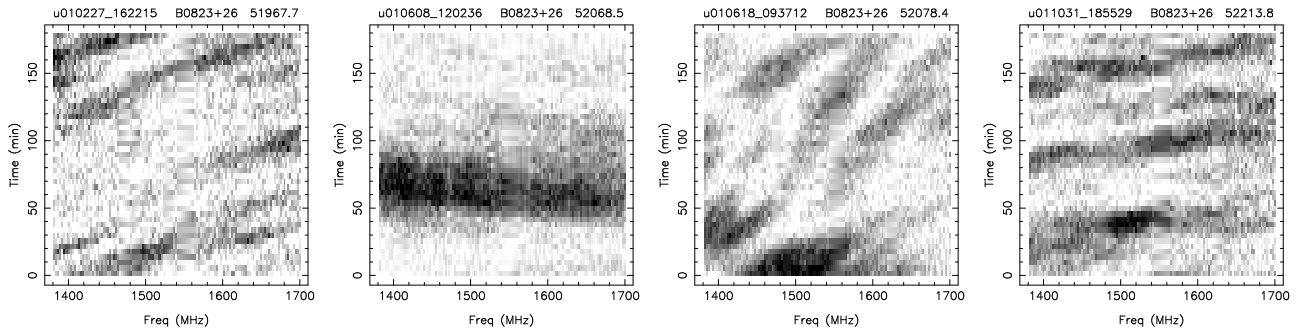


**Figure 2.** As in Fig. 1, dynamic spectra for PSR B0823+26.

distribution. There is an additional statistical error related to the finite number of scintles in the dynamic spectrum. Following Cordes, Weisberg & Boriakoff (1985), we take the fractional uncertainties in  $\Delta t_d$  and  $\Delta \nu_d$  to be given by  $N^{-0.5}$  where  $N = T_{\text{obs}} \Delta \nu_{\text{obs}} / (4 \Delta t_d \Delta \nu_d)$  is the number of observed scintles. Typical values of these additional uncertainties are

shown by error bars in the upper left corner of the  $\Delta t_d$  and  $\Delta \nu_d$  plots in Fig. 7 to 11.

Fitting for the two-dimensional Gaussian ellipse provides parameters for the sloping features of the dynamic spectrum. Following Bhat, Rao & Gupta (1999), we adopt

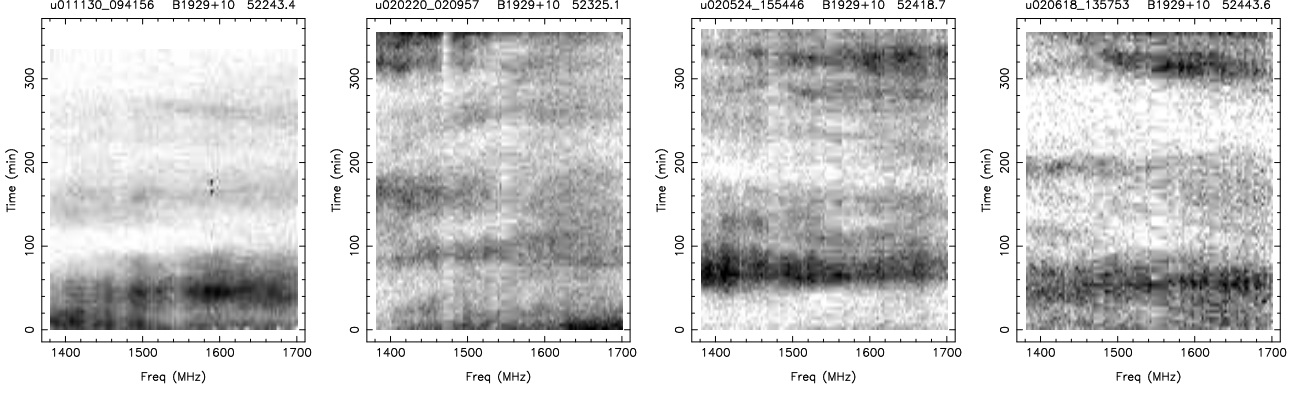


**Figure 3.** As in Fig. 1, dynamic spectra for PSR B1929+10. Note the different time scale on the vertical axis compared to Fig. 1.

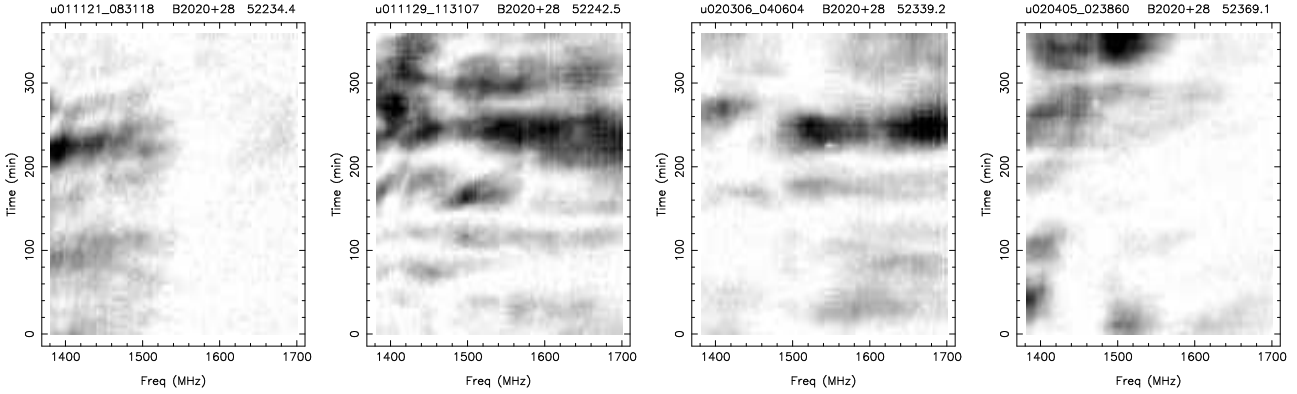


**Figure 4.** As in Fig. 1, dynamic spectra for PSR B2020+28.

$dt/d\nu$  as the drift rate; in terms of the fitted parameters  $dt/d\nu$  is given by:

$$\frac{dt}{d\nu} = - \left( \frac{C_2}{2C_3} \right). \quad (15)$$

The slope visibility  $r$  is given by:

$$r = C_2 / \sqrt{4C_1 C_3}. \quad (16)$$

Derived values for the drift rate and absolute value of slope visibility ( $|r|$ ) are plotted in Fig. 7 to Fig. 11 and average values are given in columns 5 and 6 of Table 2.

The scattering strength  $u$  is defined to be the ratio of Fresnel scale  $s_F$  to the DISS scale  $s_d$  (Rickett 1990; Gupta 1995);  $u \gg 1$  corresponds to strong scattering and  $u \ll 1$  to weak scattering. In terms of observable quantities,  $u$  is expressed as

$$u = \frac{s_F}{s_d} \sim \left( \frac{2\nu}{\Delta\nu_d} \right)^{0.5} \quad (17)$$

(Bhat, Gupta & Rao 1999), where  $\nu$  is the observing frequency. Observed mean values of  $u$  are given in column 7 of Table 2. Scattering is stronger for PSR B0329+54 compared to PSRs B0823+26, B2020+28, and B2021+51, despite their similar DMs.

Based on the simple thin screen model with power-law density fluctuations, the timescale for refractive scintillation  $t_r$  is given by

$$t_r \approx \frac{2\nu}{\Delta\nu_d} \Delta t_d \quad (18)$$

(Rickett 1990). This parameter is given in column 8 of Table 2. We use Equation 8 to estimate mean values of the fluctuation scaling parameter  $C_n^2$ ; derived values are given in column 9 of Table 2.

Pulsar velocities can be estimated from the scintillation parameters  $\Delta t_d$  and  $\Delta\nu_d$ . For a thin scattering screen placed midway between the pulsar and the observer, the transverse velocity of the pattern is given by:

$$V_s \approx 3.85 \times 10^4 \frac{\sqrt{\Delta\nu_d D}}{\nu \Delta t_d} \quad (19)$$

where  $V_s$  is in  $\text{km s}^{-1}$ ,  $\Delta\nu_d$  is in MHz, the pulsar distance  $D$  is in kpc,  $\nu$  is in GHz, and  $\Delta t_d$  is in seconds (Gupta, Rickett & Lyne 1994).  $V_s$  is a combination of the transverse velocity of the pulsar, the scattering medium and the Earth's motion. The latter two components are usually comparatively small, so  $V_s$  represents the transverse velocity of the pulsar. From Equation 19 and the parallax distances given in Table 1, we derived transverse velocities for the five pulsars. The resulting values are plotted in Fig. 7 to Fig. 11 and average values are given in column 10 of Table 2.

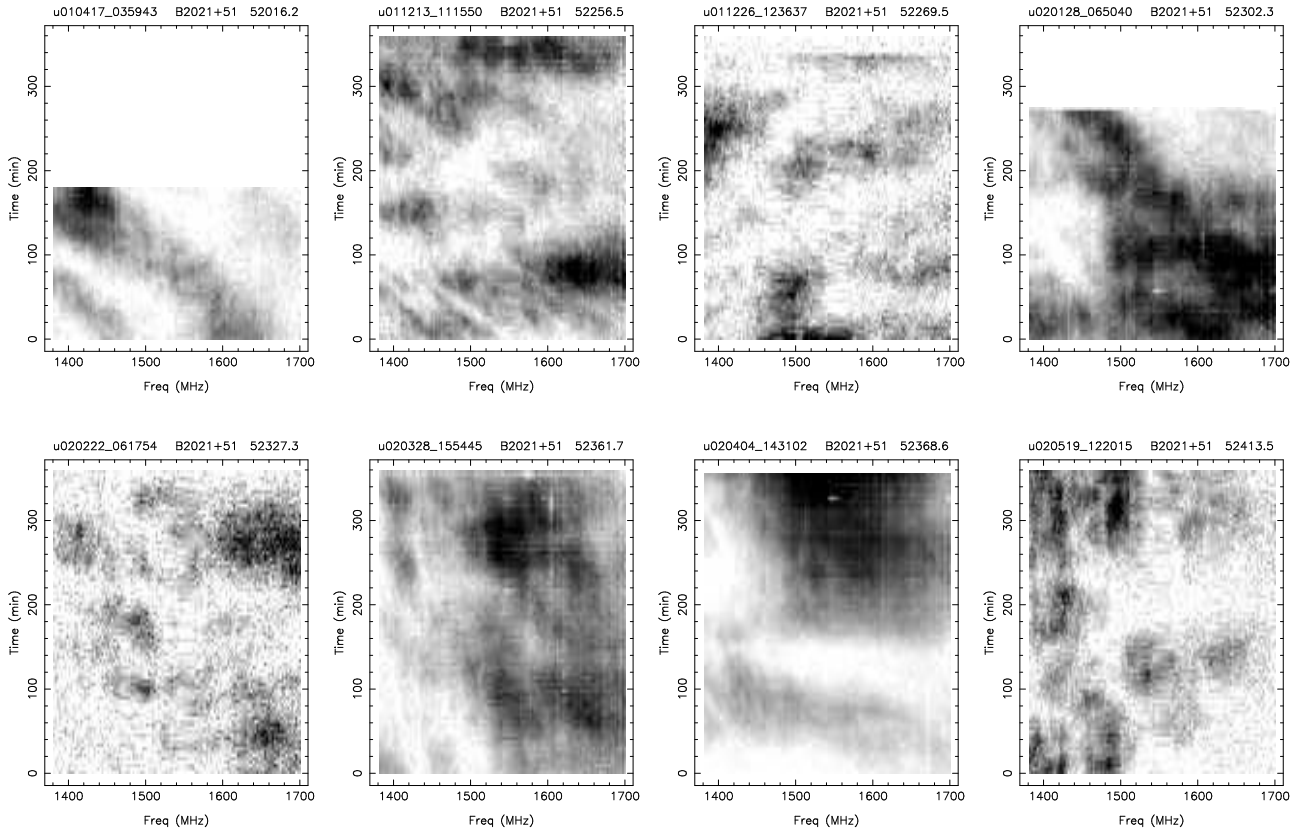


**Figure 5.** As in Fig. 1, dynamic spectra for PSR B2021+51.

### 4.3 Flux densities

Long-term observations have shown that pulsar flux density ( $S$ ) variations are dominated by refractive scintillation. Distant pulsars show little flux density variation, implying that intrinsic pulsar radio luminosities are stable (Kaspi & Stinebring 1992). Observed flux densities are plotted in Fig. 7 to Fig. 11 and mean values are given in column 11 of Table 2.

## 5 MODELLING THE ACFS

The observations of PSR B0329+54 gave us 64 independent estimates of the frequency-time correlation function of intensity. Even though these often show drifting features the average correlation function should still be estimated with good confidence and we compared it with its theoretical shape (assuming strong scattering) from a thin scattering medium with a Kolmogorov spectrum.

The theoretical intensity correlation versus spatial and frequency offsets, assuming a Kolmogorov spectrum and a thin screen, has been derived by Lambert & Rickett (1999; see their Figure 5). In Fig. 12 we compare their model with the mean of the observed auto-correlation functions, by assuming that time offsets translate simply into spatial offsets. We estimated  $\Delta\nu_d$  by fitting the theoretical shape of the cut along the frequency axis and  $\Delta t_d$  from the cut along the time axis. The observed one-dimensional correlation functions are shown by the error bars (three times the nominal standard error in the mean) with a solid line for the model.

These plots show good general agreement in shape along both axes. Particularly evident is the steeper slope near zero lag in the frequency domain than in the time domain for both the model and the observations. The minimum chi-squared value is about twice the number of data points in the fit, which maybe due to too low an estimate of the error in the mean correlation function. We suspect that the temporal variations in the two-dimensional correlations do not follow normal statistics which causes the underestimate of the error in its mean.

Whereas along the axes the model agrees with the theory, away from the axes the theory contours bulge outward more than the observed contours. The outward bulging may be related to the arc phenomenon in the secondary spectrum (see Section 6). We also note that scattering extended along the line of sight causes a reduction in the bulging effect, as can be seen in Figure 5 of Lambert & Rickett (1999).

## 6 SECONDARY SPECTRA

Secondary spectra, that is, two-dimensional Fourier transforms of dynamic spectra, give additional insight into scintillation and scattering in the interstellar medium. Fig. 13 shows secondary spectra, for several observations of PSR B0329+54 where significant fringing was observed. These spectra are much more amorphous and centrally concentrated than those shown by Hill et al. (2003) for other pulsars at a similar frequency. We note that their observations

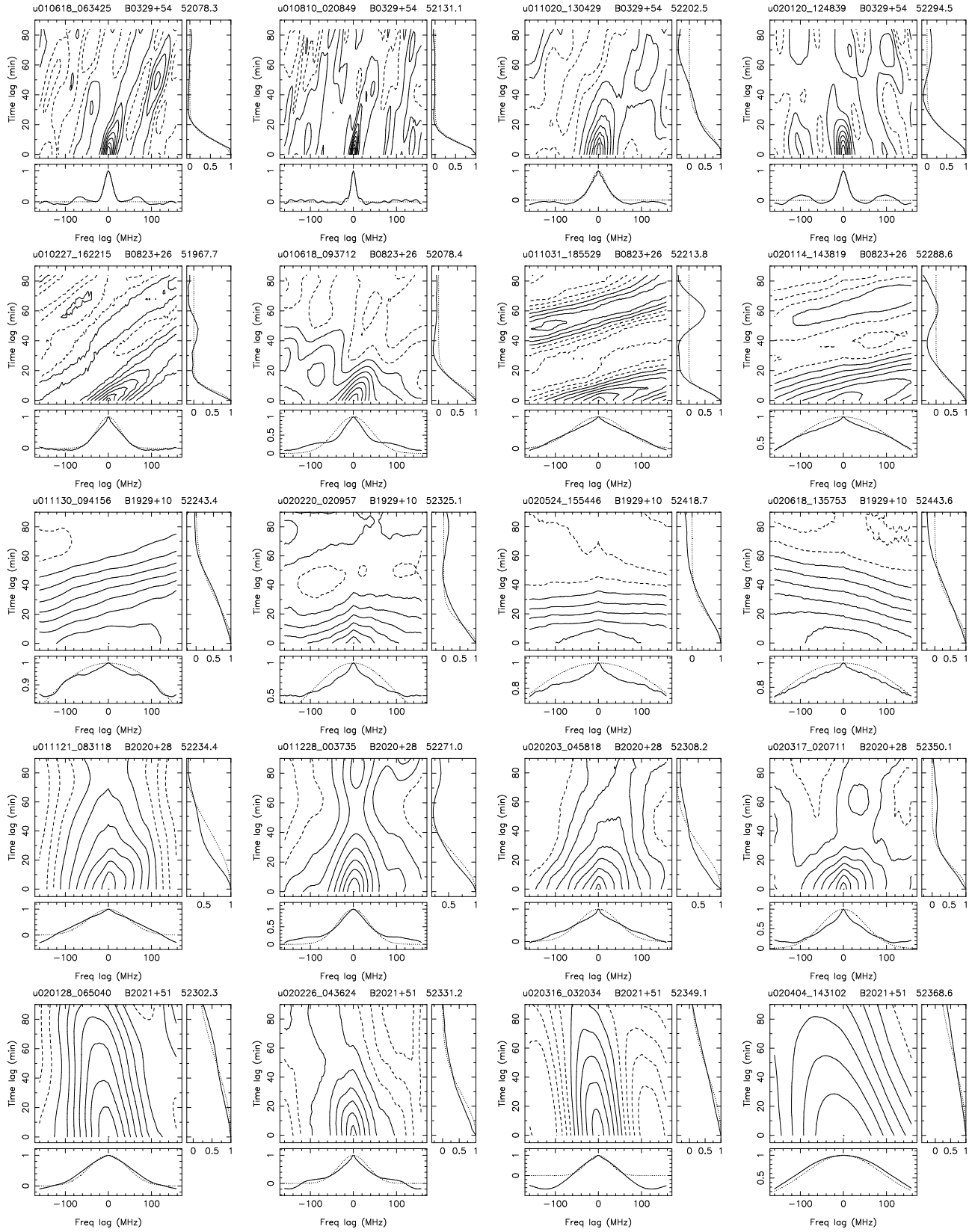


**Figure 6.** Samples of normalised two-dimensional auto-correlation functions of the dynamic spectra shown in Fig. 1 to Fig. 5. The contour interval is 0.1, with dashed lines representing negative contour levels. The solid line in the two smaller plots at the bottom and right are the one-dimensional ACFs at zero lag in time and frequency respectively. The dotted lines are zero-lag cuts through the two-dimensional Gaussian fits to the observed data.



**Table 2.** Average scintillation parameters of the observed pulsars.

PSR B	$\Delta t_d$ (min)	$\Delta \nu_d$ (MHz)	$\sigma_N$	$dt/d\nu$ (min/MHz)	$ r $	$u$	$t_r$ (day)	$\log C_n^2$	$V_s$ (km s <sup>-1</sup> )	$S$ (mJy)
(1)	(2)	(3)	(4)	(5)	(6)	(7)	(8)	(9)	(10)	(11)
0329+54	16.9(5)	14(1)	0.11	0.07(7)	0.358(3)	15	2.5	-3.0	97(5)	199(11)
0823+26	13.6(8)	82(5)	0.24	0.02(2)	0.616(6)	6	0.4	-2.8	187(9)	24(1)
1929+10	32(2)	268(24)	0.52	0.02(1)	0.442(7)	3	0.3	-3.1	136(9)	65(5)
2020+28	31(2)	70(5)	0.29	-0.01(3)	0.302(4)	7	1.0	-4.3	225(16)	40(4)
2021+51	36(3)	52(3)	0.26	-0.11(5)	0.452(4)	8	1.5	-4.0	138(8)	59(6)

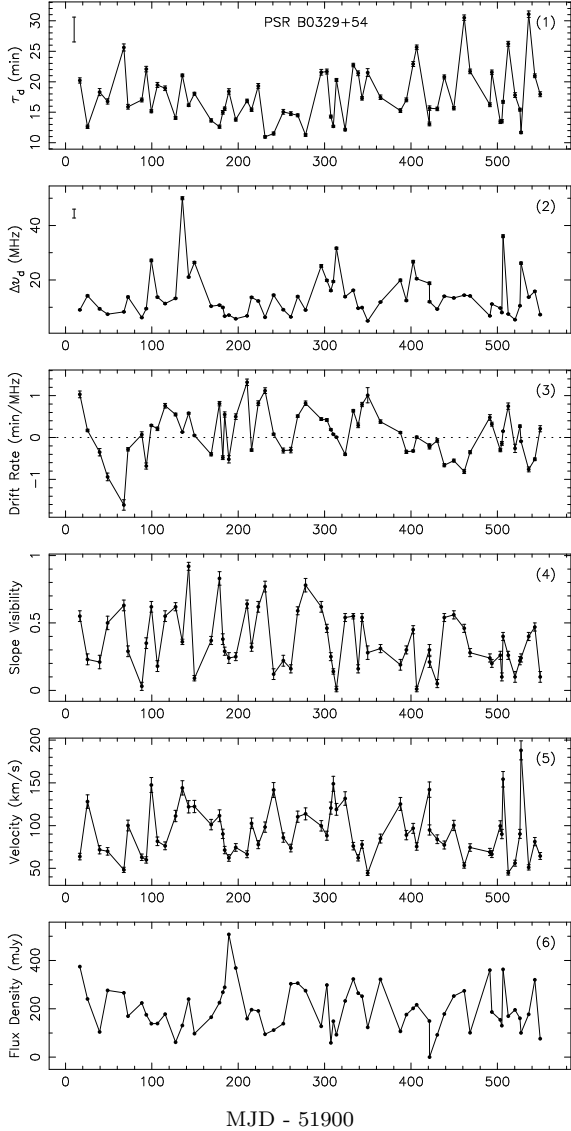


**Figure 7.** Time variations of  $\Delta t_d$ ,  $\Delta \nu_d$ , main axial angle, slope visibility, transverse velocity and the flux density for PSR B0329+54. Error bars ( $\pm 1\sigma$ ) plotted on each point are from the 2D-elliptical Gaussian fitting. The statistical uncertainty related to the finite number of observed scintles is indicated by the  $\pm 1\sigma$  error bar in the mean value shown at the top-left corner of the  $\Delta t_d$  and  $\Delta \nu_d$  plots.

have narrower bandwidths and shorter observation times but much higher time and frequency resolution (10 – 30 s and  $\sim 0.1$  MHz respectively) compared to 4 min and 2.5 MHz for our observations. Our observations therefore are sensitive to larger-scale fringes and hence smaller values of  $\theta_r$  than those of Hill et al. (2003), i.e., we are observing the central part of the scattering disk with high spatial resolution, whereas the higher-resolution observations are sensitive to large refraction angles and very fine fringing structure. Although there are some indications of rudimentary arc structure in Fig. 13, the model of interference between a strong central image and surrounding discrete images is clearly less appropriate — we are in fact observing the structure of the central image.

Across our wide observed bandwidth ( $\Delta \nu_{\text{obs}} = 320$  MHz), the frequency dependence of the slope ( $dt/d\nu \propto \nu^{-3}$ ), see Equation 9) corresponds to a 2:1 variation with larger slopes (more vertical fringes) at lower frequencies. There is some evidence for this in Fig. 1, for example, in the narrow fringing visible in the spectrum for MJD 52202.5. This slope variation will smear the corresponding feature in the secondary spectrum, contributing to the amorphous appearance of the secondary spectra (Fig. 13).

## 7 DISCUSSION

### 7.1 Dynamic spectra

For PSR B0329+54, the character of the dynamic spectra is very different from that observed at lower frequencies. Sloping fringes of different frequencies and slopes are very common in the 1540 MHz observations, whereas at lower frequencies they are uncommon (e.g., Stinebring, Faison & McKinnon, 1996). The frequency dependence of decorrelation bandwidth is directly observable within our receiver bandwidth in many dynamic spectra. Taking the observation at MJD 52294.5 for PSR B0329+54 as an example, the width of the scintle at 1400 MHz is about 13 MHz, whereas at 1640 MHz it is about 27 MHz, consistent with the prediction from Equation 7.

Despite PSRs B0329+54, B0823+26, B2020+28 and B2021+51 having very similar dispersion measures, their scintillation properties are quite different. As is well known, Galactic latitude appears to be important with stronger scattering for PSR B0329+54. Distance seems less important with very different DISS properties for PSR B0823+26 and PSR B1929+10.

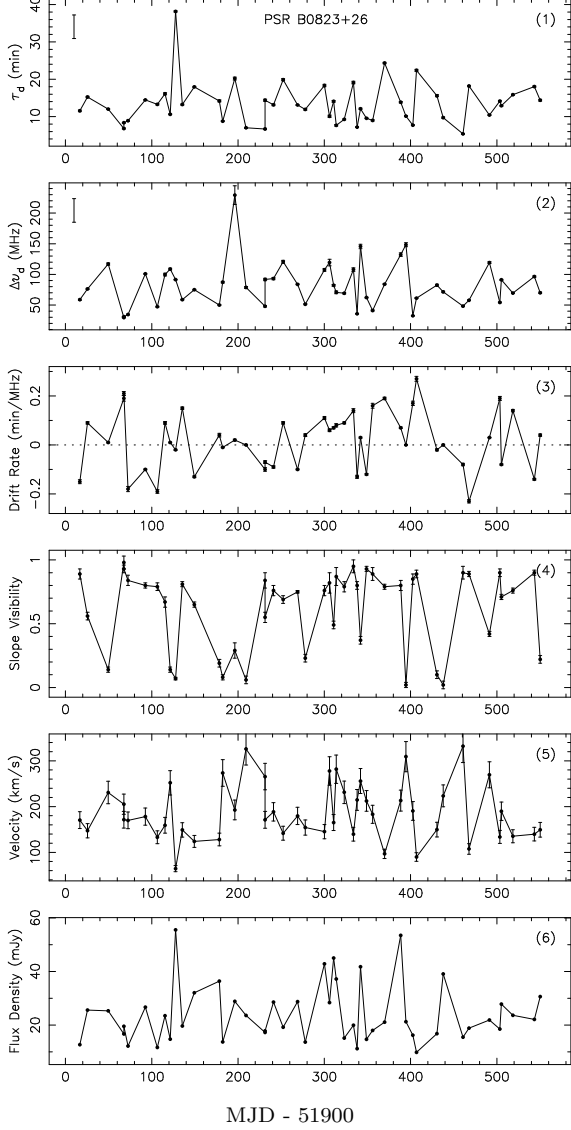


**Figure 8.** As in Fig. 7, time variations of  $\Delta t_d$ ,  $\Delta\nu_d$ , main axial angle, slope visibility, transverse velocity and the flux density for PSR B0823+26.

## 7.2 Time variations

Observed dynamic spectra vary greatly from observation to observation, in all respects: decorrelation time scale, bandwidth, brightness and the characteristics of sloping features. Fig. 7 to Fig. 11 show that scintillation parameters have a wide range of variation. For example, for PSR B0329+54 (Fig. 7), the observed diffractive timescale and decorrelation bandwidth vary over the ranges 12–30 min and 5–34 MHz respectively. Similar variations are observed for the other four pulsars. The interval between observations is typically several times the refractive timescale  $t_r$  (Table 2) and so we would expect uncorrelated variations. However, the expected modulation due to refractive scintillation can only account for a small amount of the observed variations. Modulation indices (ratio of rms deviation to mean value) for the variations in  $\Delta t_d$ ,  $\Delta\nu_d$  and flux density,  $m_t$ ,  $m_b$  and  $m_r$  respectively, are given in Table 3. Also given in the Table are pre-

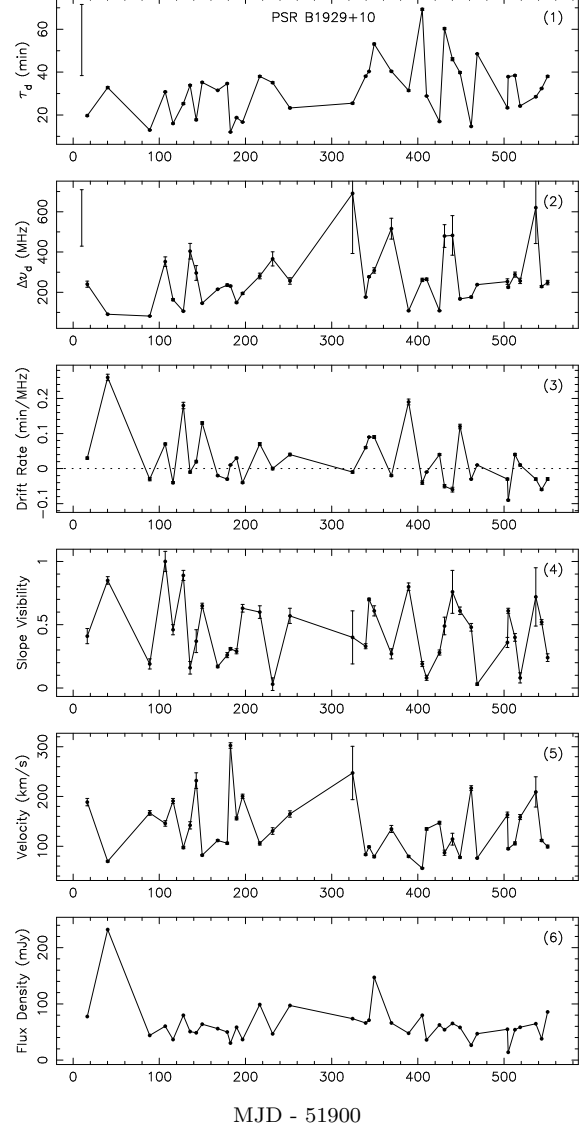


**Figure 9.** As in Fig. 7, time variations of  $\Delta t_d$ ,  $\Delta\nu_d$ , main axial angle, slope visibility, transverse velocity and the flux density for PSR B1929+10.

dicted modulation indices for the case of a thin screen with a Kolmogorov density spectrum ( $\beta = 11/3$ ) and strong scattering (Romani, Narayan & Blandford 1986; Bhat, Gupta & Rao 1999). In all cases, the observed modulation indices are greater than the predicted values. With our relatively high observing frequency and relatively nearby pulsars, the scattering strength  $u$  is only modestly greater than one, so the strong scattering assumption is not really satisfied. Also, the form of the variations suggests that large-scale fluctuations in the screen are important, so the fluctuation spectrum is likely to be steeper than in the Kolmogorov case.

Fig. 7 to Fig. 11 show that there are significant correlated changes in decorrelation time-scale, bandwidth and drift rate over intervals of several weeks and in some cases many months, much larger than the predicted refractive timescale  $t_r$ . For example, in Fig. 7 for PSR B0329+54, there are high values of decorrelation bandwidth at MJD 52035

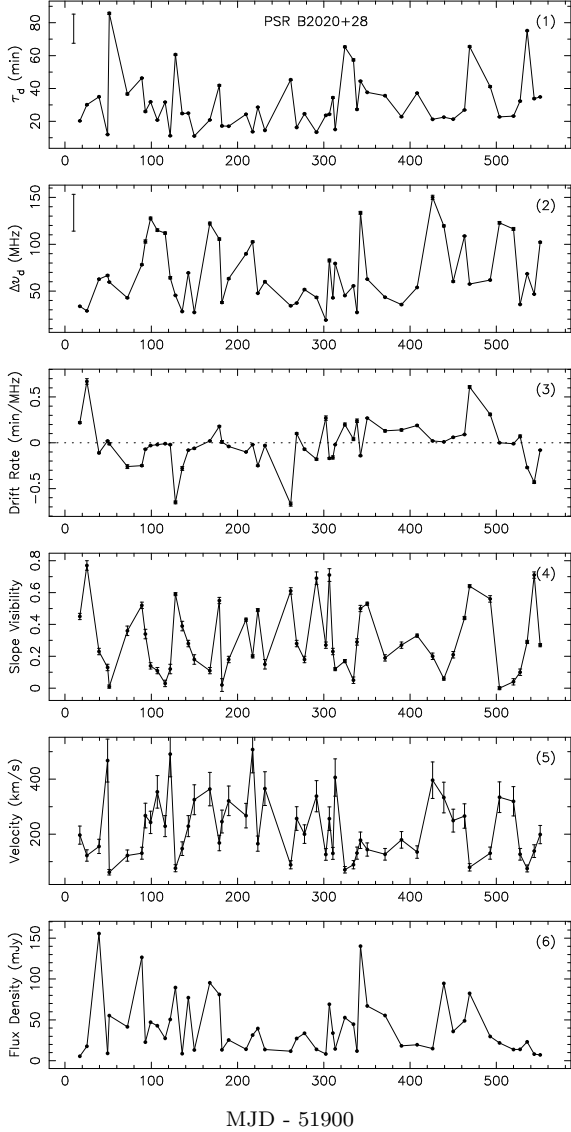


**Figure 10.** As in Fig. 7, time variations of  $\Delta t_d$ ,  $\Delta\nu_d$ , main axial angle, slope visibility, transverse velocity and the flux density for PSR B2020+28.

and 52287, low values of drift rate between MJD 52295 and 52370, an increase and then decrease in slope visibility between MJD 52160 and 52215 and larger than average flux densities between 52050 and 52110. These results show that gradients in refractive index of scale much larger than that of the diffractive scattering disk exist in the scattering screen.

In general, there is little correlation between variations in the various parameters. However, there are exceptions. For example, Fig. 11 shows a very significant correlation between decorrelation time-scale and flux density. As remarked in Section 4.2, the pulsar tends to be strong when the scintillation timescale is long. This suggests that most of energy from the pulsar is confined to the central region of the scattering disk where the scattering angles are small, leading to broad scintles. Only when we are in a null of these broad patterns do we see weaker radiation from outer parts of the

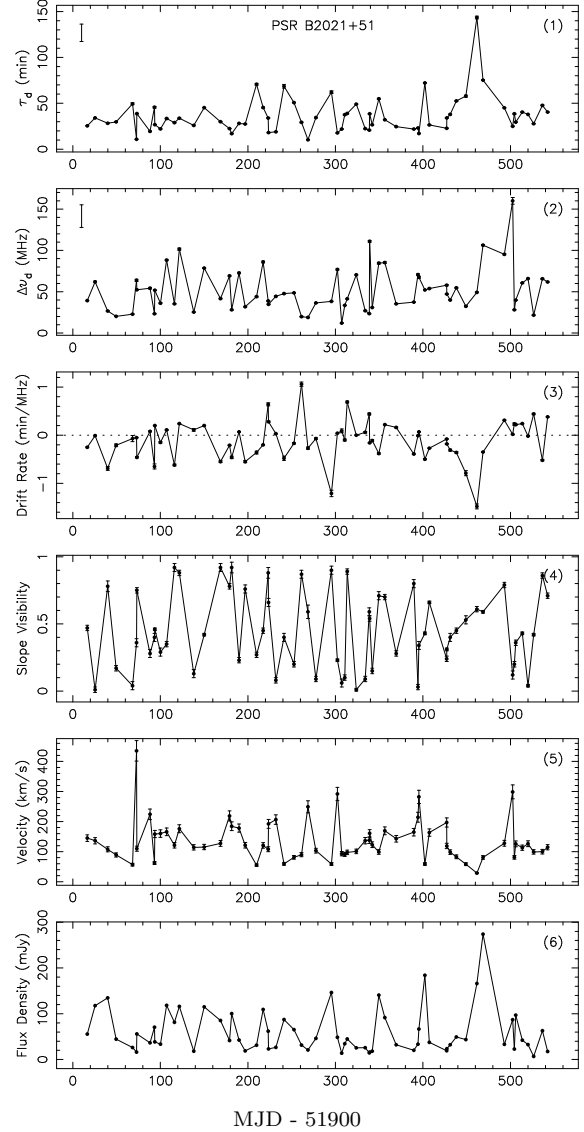


**Figure 11.** As in Fig. 7, time variations of  $\Delta t_d$ ,  $\Delta\nu_d$ , main axial angle, slope visibility, transverse velocity and the flux density for PSR B2021+51.

scattering disk where scattering angles are larger and scintles are smaller.

Due to the wide range variation of diffractive timescale and decorrelation bandwidth, the derived velocity is also highly variable. However, there is remarkably good agreement of the average scintillation velocities (Table 2) with the velocities derived from proper motion measurements (Table 1). We attribute this to our long-term observations which averaged over the refractive scintillation modulations (Bhat, Rao & Gupta 1999). This agreement also indicates that locating a thin screen approximately half-way between the pulsar and observer is a good assumption (Gupta, Rickett & Lyne 1994; Nicastro et al. 2001).

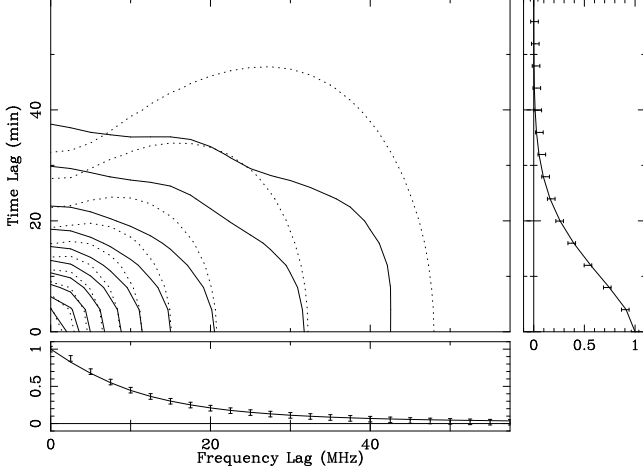


**Figure 12.** Auto correlation versus frequency and time lag for PSR B0329+54. Solid contours for the average auto correlation of 64 individual observations. Dashed lines are contours for a Kolmogorov model in the diffractive limit of scattering from a thin screen.  $\Delta\nu_d$  and  $\Delta t_d$  were fitted to the cuts along the axes as displayed in the two small bottom and right plots, where the data are represented by error bars that are three times the nominal standard error in the mean. Notice how the dashed contours agree with the solid contours on each axis, but bulge out away from the axes.

**Table 3.** Modulation indices for  $\Delta t_d$ ,  $\Delta\nu_d$  and flux density.

PSR B (1)	$m_t$ (2)	$m_{t,th}$ (3)	$m_b$ (4)	$m_{b,th}$ (5)	$m_r$ (6)	$m_{r,th}$ (7)
0329+54	0.26	0.08	0.74	0.16	0.47	0.23
0823+26	0.43	0.11	0.45	0.23	0.45	0.32
1929+10	0.41	0.13	0.54	0.28	0.57	0.36
2020+28	0.53	0.10	0.48	0.21	0.87	0.23
2021+51	0.55	0.10	0.52	0.20	0.83	0.24

### 7.3 Power spectrum of electron density turbulence

The frequency dependence of the DISS parameters can be used to estimate the spectral slope of interstellar turbulence. Table 4 shows the results from earlier low-frequency observations, with the data in columns 2 and 3 derived from observations using the Ooty Radio Telescope at 327 MHz by Bhat, Rao & Gupta (1999), columns 4 and 5 are from 408 MHz observations by Gupta, Rickett & Lyne (1994) and columns 6 and 7 are from 610 MHz observations by Stinebring, Faison & McKinnon (1996). For convenience, columns 8 and 9 are from our observations, repeated from Table 2. For Kolmogorov turbulence, the frequency dependences of scintillation parameters are given by:  $\Delta t_d \propto \nu^{1.2}$ ,  $\Delta\nu_d \propto \nu^{4.4}$  (see Equations 4 and 7). Scintillation timescales are in reasonable accord with the predicted frequency dependence, but the observed values of the decorrelation bandwidth are systematically lower at high frequencies. Fitting for the observed time scale and decorrelation bandwidth we obtained the power index,  $\alpha_t$  and  $\alpha_\nu$  and the corresponding density spectral indices  $\beta_t$  and  $\beta_\nu$ , using a model for a density fluctu-

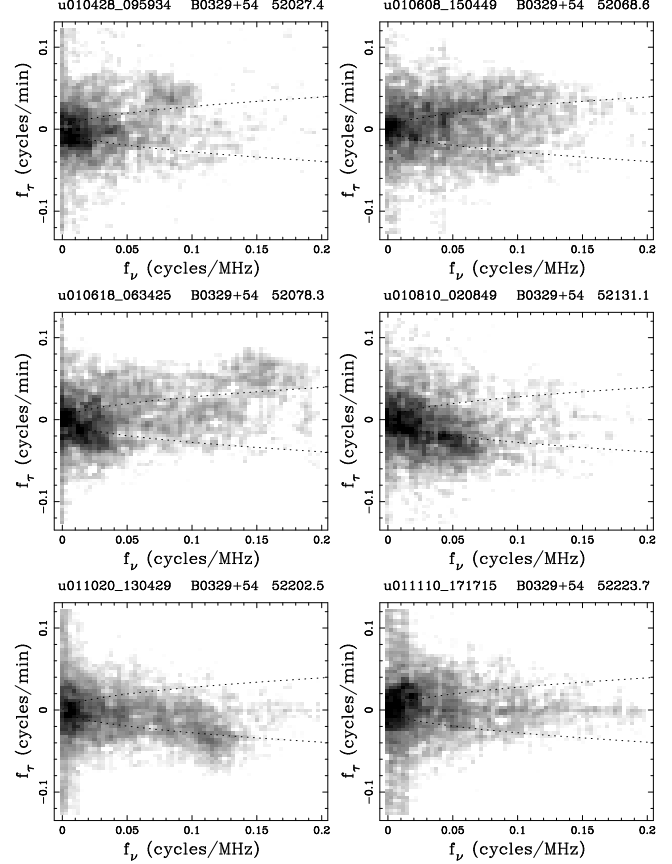


**Figure 13.** Secondary spectra for selected observations of PSR B0329+54. The spectra have been Hanning weighted to reduce sidelobes and improve the signal/noise ratio. The dotted lines indicate expected arcs derived from Equation 8.

ation spectrum with  $\beta < 4$  (Equations 2 & 5). These values, shown in the last four columns in Table 4 (except in one case) show a flatter frequency dependence for  $\Delta t_d$  and  $\Delta\nu_d$  than predicted, implying a density fluctuation index much larger than the Kolmogorov value and in fact greater than the critical value of four. We therefore applied a model for a steeper density fluctuation spectrum,  $\beta > 4$  (Equations 3 & 6). However, the derived values contradict the assumption giving  $\beta_t < 4$  and  $\beta_\nu < 4$ .

The flat frequency dependence of  $\Delta t_d$  and  $\Delta\nu_d$  is not predicted by either theory. Similar low values of  $\alpha_\nu$  were also observed earlier by Johnston, Nicastro & Koribalski (1998) and Löhmer et al. (2001). The former work consists of multi-frequency DISS observations for large sample of pulsars and in the latter paper the index was derived from scatter broadening observations. This result may imply a relatively small outer scale for the scattering fluctuations or may be a consequence of weaker scattering at the higher frequencies.

By comparing the diffractive and refractive scattering angles,  $\theta_d$  and  $\theta_r$  respectively, we can estimate the spectral index  $\beta$  of the density fluctuations (Equation 1). In terms of observable quantities, they are given by

$$\theta_d = \left( \frac{c}{\pi D \Delta\nu_d} \right)^{0.5}, \quad (20)$$

**Table 4.** Fitting for frequency dependences of  $\Delta t_d$  and  $\Delta \nu_d$  and the corresponding density spectra.

Obs. Freq	327 MHz <sup>a</sup>		408 MHz <sup>b</sup>		610 MHz <sup>c</sup>		1540 MHz <sup>d</sup>		$\alpha_t$	$\beta_t$	$\alpha_\nu$	$\beta_\nu$
PSR B	$\Delta t_d$ (min)	$\Delta \nu_d$ (MHz)	$\Delta t_d$ (min)	$\Delta \nu_d$ (MHz)	$\Delta t_d$ (min)	$\Delta \nu_d$ (MHz)	$\Delta t_d$ (min)	$\Delta \nu_d$ (MHz)				
(1)	(2)	(3)	(4)	(5)	(6)	(7)	(8)	(9)	(10)	(11)	(12)	(13)
0329+54	5.1	0.165	3.2	0.046	5.9	0.349	16.9	14	0.93	4.2	3.3	5.0
0823+26	4.2	0.293	1.7	0.269			13.6	82	1.00	4.0	3.9	4.1
1929+10	5.8	1.293					32	268	1.10	3.8	3.4	4.8
2020+28	4.7	0.270					31	70	1.22	3.6	3.6	4.5
2021+51							36	52				

<sup>a</sup> Bhat, Rao & Gupta 1999<sup>b</sup> Gupta, Rickett & Lyne 1994<sup>c</sup> Stinebring, Faison & McKinnon 1996<sup>d</sup> Our Results

and Equation 9 rearranged

$$\theta_r = \left( \frac{V_s \nu}{D} \right) \left( \frac{dt}{d\nu} \right), \quad (21)$$

where  $V_s$  is given in Table 2 and  $dt/d\nu$  is the drift slope of the dynamic spectrum from Equation 15. The mean values of  $\langle \theta_d \rangle$  and  $\langle \theta_r \rangle$  are given in columns 2 and 3 of Table 5. As expected for random fluctuations in the scattering medium,  $\langle \theta_r \rangle$  is essentially zero within the uncertainties. However, the scale of the refractive scattering can be estimated from the rms fluctuation of  $\theta_r$ , denoted as  $\sigma_{\theta_r}$  and given in column 4 of Table 5. Following Bhat, Gupta & Rao (1999) we scale this quantity by a factor of  $\sqrt{2}$  to allow for mis-alignment of the refractive gradient and the pattern velocity.

We estimate the spectral index of the electron density fluctuations using

$$\beta = 4 + \left[ \frac{\log(\sigma_{\theta_r} / \langle \theta_d \rangle)}{\log u} \right], \quad (22)$$

where  $u$  is the measurement of scattering strength defined in Equation 17 (Bhat, Gupta & Rao 1999). This formula indicates that  $\sigma_{\theta_r} < \langle \theta_d \rangle$  corresponds to a flatter spectrum  $\beta < 4$  but  $\sigma_{\theta_r} > \langle \theta_d \rangle$  corresponds to a steeper spectrum  $\beta > 4$ . In our case as  $\sigma_{\theta_r} \ll \langle \theta_d \rangle$ , and the measured  $\beta$  are in the range 3.40 – 3.75, on average somewhat less than the Kolmogorov spectrum index of 3.67, but in most cases consistent with it.

Taken at face value, these results are inconsistent with those based on the frequency dependence of scintillation parameters (Table 4). One possible explanation is that the fluctuations at the diffractive and refractive scales are independent, not related by the cascade of turbulent energy and hence not described by the Kolmogorov spectrum (Armstrong, Rickett & Spangler 1995). We also note that our range of derived drift slopes is limited by the observing parameters, especially time and frequency resolution. Higher resolution observations (e.g. Hill et al. 2003) detect a wider range of slopes and hence imply larger refractive angles and a steeper spectrum for the density fluctuations.

**Table 5.** Estimates of diffractive and refractive scattering angles, and the spectral index of electron density fluctuation.

PSR B	$\langle \theta_d \rangle$ (mas)	$\langle \theta_r \rangle$ (mas)	$\sigma_{\theta_r}$ (mas)	$\beta$
(1)	(2)	(3)	(4)	(5)
0329+54	0.106(3)	0.005(3)	0.036	3.59
0823+26	0.070(2)	0.004(5)	0.044	3.75
1929+10	0.043(2)	0.003(2)	0.019	3.33
2020+28	0.029(1)	−0.0003(9)	0.009	3.40
2021+54	0.039(1)	−0.002(2)	0.017	3.61

## 8 SUMMARY

In this paper we present dynamic spectra for PSRs B0329+54, B0823+26, B1929+10, B2020+28 and B2021+51 over a 320 MHz centred at 1540 MHz. The time and frequency bandwidth resolutions are 4 min and 2.5 MHz respectively. The dynamic spectra show different features compared to earlier lower-frequency observations. For example, PSR B0329+54 presents frequent drifting patterns and fringes which were not seen at lower frequencies. Our individual observations are generally long enough to cover at least a few scintles, but in some cases, especially for PSR B1929+10, the scintles are wide compared to our bandwidth. In these cases, the value of  $\Delta \nu_d$  is based on just the peak of the ACF and is rather uncertain. Although the observations show a wide range of variations in diffractive scintillation parameters, the average scintillation velocities are in good agreement with the proper motion velocities.

The frequency and time correlations are successfully described by theory for a thin Kolmogorov scattering screen. However, there is a consistent disagreement for points off the axes, which suggests turbulence extended along the line of sight. There is also much greater variability than expected in the shapes of the daily auto-correlations, which suggests a stronger than expected influence of scales larger than the scattering disc. We note here that similar conclusion has been drawn by Lambert & Rickett (2000), Spangler (2001) and Shishov et al. (2003). These authors also pointed to more complex models than a Kolmogorov thin screen. We

do not have theoretical predictions for the full frequency-time correlation for the implied steeper spectrum models, which thus becomes an area for future work.

With our wide observed bandwidth, long observation times and lower time and frequency resolution, our observations are sensitive to larger-scale fringes and hence smaller refractive angles, corresponding to the central part of the scattering disk. The secondary spectra we obtained for PSR B0329+54 are centrally concentrated and rather amorphous. Some of the smearing results from a  $\nu^{-3}$  frequency dependence of fringe slope across our wide observed band.

Modulations in time scale, decorrelation bandwidth and flux density are greater than predictions from a thin screen model with a Kolmogorov spectrum of density fluctuations. The long-term variations in DISS parameters suggests larger-scale density fluctuations exist, corresponding to a steeper fluctuation spectrum. Comparison of the observed DISS timescales with values extrapolated from lower frequency measurements based on the Kolmogorov spectrum show good agreement. However, large discrepancies were found in extrapolated decorrelation bandwidths, with the observed values substantially smaller than the predicted values. This gives a flatter frequency dependence of decorrelation bandwidth, corresponding to a steeper density fluctuation spectrum.

In contrast, estimation of the power-law density fluctuation index  $\beta$  from diffractive and refractive scattering angles gives a value in the range 3.40 – 3.75, on average smaller but consistent with a Kolmogorov spectrum. The range of derived drift slopes is limited by the observing parameters, and observations with higher resolution will detect larger refractive angles and hence imply a steeper density spectrum. It is also possible that the large-scale fluctuations responsible for refractive effects are not directly related to the smaller-scale fluctuations responsible for diffractive scintillation.

## ACKNOWLEDGMENTS

We thank the engineers of Urumqi Observatory who help with maintaining the system, we also thank those who helped with the observations. NW thanks the support from NNSFC under the project of 10173020. We thank Mark Walker for his helpful suggestions and discussions.

## REFERENCES

- Armstrong J. W., Rickett B. J., Spangler S. R., 1995, *ApJ*, 443, 209
- Bhat N. D. R., Gupta Y., Rao A. P., 1999, *ApJ*, 514, 249
- Bhat N. D. R., Rao A. P., Gupta Y., 1999, *ApJS*, 121, 483
- Blandford R. D., Narayan R., 1985, *MNRAS*, 213, 591
- Briskin W. F., Benson J. M., Goss W. M., Thorsett S. E., 2002, *ApJ*, 571, 906
- Coles W. A., Frehlich R. G., Rickett B. J., Codona J. L., 1987, *ApJ*, 315, 666
- Cordes J. M., 1986, *ApJ*, 311, 183
- Cordes J. M., Pidwerbetsky A., Lovelace R. V. E., 1986, *ApJ*, 310, 737
- Cordes J. M., Weisberg J. M., Boriakoff V., 1985, *ApJ*, 288, 221
- Goodman J., Narayan R., 1985, *MNRAS*, 214, 519
- Gupta Y., 1995, *ApJ*, 451, 717
- Gupta Y., Rickett B. J., Coles W. A., 1993, *ApJ*, 403, 183
- Gupta Y., Rickett B. J., Lyne A. G., 1994, *MNRAS*, 269, 1035
- Gwinn C. R., Taylor J. H., Weisberg J. M., Rawley L. A., 1986, *AJ*, 91, 338
- Hewish A., 1980, *MNRAS*, 192, 799
- Hewish A., Wolszczan A., Graham D. A., 1985, *MNRAS*, 213, 167
- Hill A. S., Stinebring D. R., Barnor H. A., Berwick D. E., Webber A. B., 2003, *ApJ*, 599, 457
- Johnston S., Nicastrò L., Koribalski B., 1998, *MNRAS*, 297, 108
- Kaspi V. M., Stinebring D. R., 1992, *ApJ*, 392, 530
- Lambert H. C., Rickett B. J., 1999, *ApJ*, 517, 299
- Lambert H. C., Rickett B. J., 2000, *ApJ*, 531, 883
- Löhmer O., Kramer M., Mitra D., Lorimer D. R., Lyne A. G., 2001, *ApJ*, 562, L157
- Lyne A. G., Anderson B., Salter M. J., 1982, *MNRAS*, 201, 503
- Nicastrò L., Nigro F., D’Amico N., Lumiella V., Johnston S., 2001, *A&A*, 368, 1055
- Rickett B. J., 1977, *Ann. Rev. Astr. Ap.*, 15, 479
- Rickett B. J., 1990, *Ann. Rev. Astr. Ap.*, 28, 561
- Romani R. W., Narayan R., Blandford R., 1986, *MNRAS*, 220, 19
- Shishov V. I. et al., 2003, *A&A*, 404, 557
- Spangler S. R., Gwinn C. R., 1990, *ApJ*, 353, L29
- Spangler S. R., 2001, *Space Sci. Rev.*, 99, 261
- Stinebring D. R., Faison M. D., McKinnon M. M., 1996, *ApJ*, 460, 460
- Stinebring D. R., McLaughlin M. A., Cordes J. M., Becker K. M., Goodman J. E. E., Kramer M. A., Sheckard J. L., Smith C. T., 2001, *ApJ*, 549, L97
- Wang N., Manchester R. N., Zhang J., Wu X. J., Yusup A., Lyne A. G., Cheng K. S., Chen M. Z., 2001, *MNRAS*, 328, 855
- Wolszczan A., Cordes J. M., 1987, *ApJ*, 320, L35